Title
Electron small polarons and their mobility in iron (oxyhydr)oxide nanoparticles

Permalink
https://escholarship.org/uc/item/7c07340b

Author
Katz, J.E.

Publication Date
2012-08-01

DOI
DOI: 10.1126/science.1223598

Structure and surface charge controlled small-polaron mobility in iron oxide and oxyhydroxide nanoparticles

Jordan E. Katz[1,2,‡], Xiaoyi Zhang[3], Klaus Attenkofer[3], Karena W. Chapman[3], Cathrine Frandsen[4], Piotr Zarzycki[5,6], Kevin M. Rosso[5], Roger W. Falcone[2], Glenn A. Waychunas[1] and Benjamin Gilbert[1,*]

[1]*Earth Sciences Division, Lawrence Berkeley National Laboratory.*

[2]*Department of Physics, University of California – Berkeley.*

[3]*X-ray Science Division, Argonne National Laboratory.*

[4]*Department of Physics, Technical University of Denmark.*

[5]*Chemical and Materials Sciences Division, Pacific Northwest National Laboratory*

[6]*Institute of Physical Chemistry, Polish Academy of Sciences, Warsaw, Poland.*

‡ Current address: Department of Chemistry, Denison University.

* Corresponding author: BGilbert@lbl.gov

Redox-active transition metal (TM) oxide, hydroxide and oxyhydroxide semiconductors typically posses wide *p-d* charge-transfer band gaps and exhibit poor charge carrier mobility. Nevertheless, there is increasing evidence that electron mobility within TM (oxyhydr)oxides is a crucial feature of their redox reactivity, affecting the rates of interfacial reactions, the outcomes of redox-driven phase transformations and enabling charge transfer between reactions occurring at widely-separated surface sites [1,2]. In order to determine the links between crystal structure and charge transport efficiency on solid-phase redox reactivity we have applied a pump-probe method to observe directly the fate of electrons introduced into ferric

iron (oxyhydr)oxide nanoparticles via ultrafast interfacial electron transfer[3]. Using time-resolved X-ray spectroscopy, we observed the formation of reduced and structurally distorted metal sites consistent with small polarons. By tracking the lifetime of the reduced metal states, rate constants for thermally-activated cation-to-cation electron hopping in the solid can be measured with subnanosecond precision. Hopping-mediated electron conduction in maghemite involves both octahedrally and tetrahedrally-coordinated iron sites. Comparisons between different phases revealed that short-range structural topology, not long-range order, dominates the electron-hopping rate, and shed new insight into the structure and properties of the naturally-formed nanomaterial, ferrihydrite[4]. Lattice Monte Carlo simulations revealed that, on timescales relevant to solid-phase reactions, surface charge plays a commanding role in biasing electron conduction trajectories.

The redox chemistry of many TM (oxyhydr)oxides is central to their roles and impacts in environmental[5], technological[6,7] and biological[8] settings and exhibits rich behavior due to the coupling of redox and conduction processes. The electrical properties of these semiconductor materials are dominated by short-range metal-ligand bonding[9]. Theoretical calculations predict that conduction states are highly localized and that strong electron-phonon interactions stabilize charge carriers in a lattice distortion, forming mid-gap polaronic states[10,11]. In particular, excess electrons occupying partially-filled TM *3d* states tend to self-localize as metal-centered small polarons. Electron mobility in the small-polaron model occurs through thermally-activated electron hopping from one metal site to the next in a process akin to a valence interchange electron-transfer (ET) reaction. The small-polaron model is widely used for describing thermally activated conduction in semiconductors, but the extent to which it provides an accurate description of charge carriers at a structural level has never been experimentally verified. Transport characteristics are most commonly assessed using temperature-dependent measurements of the bulk conductivity within complex polycrystalline materials, *e.g.*, with pressed pellets[12,13]. If Arrhenius analysis reveals the existence of an activation-energy for charge transport, phenomenological macroscopic transport models allow an elementary hopping rate to be inferred. More rarely, measurements of charge carrier mobilities within structurally well-defined individual metal oxide crystals have been performed[12], but do not directly evaluate the existence of small polarons. Transient optical absorption studies can measure the lifetime of electron-hole pairs generated by light absorption[14], but does not reveal the mobility of any photogenerated charge carriers.

We have developed a pump-probe approach to study the nature and dynamics of charge-carrying electrons in ferric iron phases at multiple timescales[3]. The method uses laser-initiated interfacial ET to reduce a fraction of iron atoms at the surface of ferric (Fe^{3+}) iron (oxyhydr)oxide nanoparticles sensitized by the photoactive dye molecule 2',7'-dichlorofluorescein (27DCF). This approach is inspired by research on dye-sensitized semiconductor nanomaterials[15] and informed by numerous accomplishments in ultrafast science, including optical-pump–X-ray probe studies of transient electronic and structural configurations in metal-organic cluster compounds at temporal resolutions exceeding 250 femtoseconds[16-18]. UV-pump–X-ray probe studies have been used to study a single photochemical reaction of iron, ferrioxalate photolysis[19]. Here we report the results of studies of the mobility of excess electrons introduced into three phases of ferric iron (oxyhydr)oxide: two crystalline phases, 3.4-nm maghemite and 7-nm hematite (α-Fe_2O_3), and ~3-nm 2-line ferrihydrite, an important environmental[4] and physiological[8] nanophase. Synthesis methods were optimized to achieve the smallest size nanoparticles without impurity phases, as confirmed by X-ray diffraction and electron microscopy (**Figs. S1-5**). Nanoparticle samples were studied in aqueous suspension at pH 4 with or without surface-bound 27DCF.

Figure 1a illustrates expected pathways following light initiated ET. We used transient absorption (TA) spectroscopy with 520-nm wavelength excitation and visible probe wavelengths to characterize the optical excitations of the nanoparticles and the light-initiated interfacial ET step, finding similar behavior for all phases. All uncoated nanoparticles gave an optical TA response with a lifetime less than 200 ps that could be fitted by a two-exponential decay function. This transient signal represents the creation of electron-hole pairs that recombine via non-radiative transitions[14]. **Figures 2a & b** display TA kinetics data and global fit analysis for 27DCF-coated hematite nanoparticles at selected optical probe wavelengths. The transient spectra contain contributions from absorption of the oxidized dye; stimulated emission from excited state of the dye prior to interfacial ET; ground-state bleaching of the dye; and excited state transitions of trapped photoelectrons generated by band-gap absorption in the nanoparticles, independent of the dye (see discussion in **Supplementary Information**). Global analysis incorporated the optical TA decay rates obtained from fits to the uncoated nanoparticles (characterizing the band-gap excitations) and four additional exponential decay components (associated with dye excitation, interfacial ET, and recombination). For all 27DCF-coated nanoparticles, the fastest time constant (200 – 250 fs) was associated with a transient spectrum consistent with stimulated emission, demonstrating that interfacial ET occurred on a subpicosecond timescale, as observed for TiO_2 (ref. 20). Thus interfacial ET is much faster than any subsequent spontaneous ET processes, described below, that are relevant to electron transport in iron (oxyhydr)oxide nanoparticles.

We performed time-resolved X-ray absorption spectroscopy (XAS) to characterize the solid-phase species generated by interfacial ET. Fe K-edge XAS is a sensitive probe of the oxidation state and coordination geometry of solid phase, complexed or dissolved iron[21], and has been used to study transient iron species in pump-probe studies[16,22]. For each sample, **Figure 3a** shows ground state Fe K-edge XAS spectra and **Figure 3b** shows transient XAS spectra acquired 150 ps following ET, reported as difference X-ray absorption (ΔXA) spectra. Although the magnitudes of the ΔXA spectra are small (~1% of total signal) these spectra were observed reproducibly during our studies of dye-sensitized nanoparticles. No transient spectrum was detectable for any control (**Fig. S11**). XAS analysis and chemical assays of the samples after reaction showed the accumulation of dissolved ferrous iron (**Figs. S5 & S12b**).

The position of the dominant feature of all ΔXA spectra indicates that the spectra of the transient iron species shifted to lower energy, consistent with a model in which light-initiated ET reduced Fe^{3+} to Fe^{2+} (ref. 21). The ferrous/ferric K-edge chemical shift for iron that is octahedrally coordinated by oxygen is typically observed to be -1.4 ± 0.1 eV (ref. 23). Thus, we created trial ΔXA spectra for iron reduction without structural change by applying this energy shift to a copy of the ground state spectra and mixing it at a 1% level with the original. The resulting spectra do not match the experimental transient spectra well for any phase, indicating that structural change accompanies reduction. Since the chemical reduction of both maghemite[24] and ferrihydrite[25] can cause transformation to the mixed valence inverse spinel magnetite, Fe_3O_4, we tested whether light-initiated ET led to the formation of magnetite domains but obtained poor matches to the experimental data. Magnetite and maghemite differ in oxygen stoichiometry as well as iron valence, and thus the poor agreement indicates that atom diffusion to achieve local charge balance and the nucleation of a new mineral phase does not occur within 150 ps (ref. 26). Thus, interfacial ET causes iron reduction and a structural change that is less extensive than complete phase change.

We developed a theoretical approach to test whether the transient spectra observed for hematite and maghemite are consistent with the formation of small polarons in these phases. We used *ab initio* calculations for periodic systems to predict the distortion in the local structure of a ferrous iron site using methods similar to previous work[11]. Briefly, an extra electron was localized on an iron cation in the ground state, and all atomic coordinates were energy minimized self-consistently with the wave function until converged. The small polaron structure was defined relative to the atomic coordinates calculated for a completely ferric lattice. The consequences for structural distortion on XAS were investigated using a full multiple scattering code[27] that has been used successfully to interpret metal K-edge spectra[28]. Simulation parameters were chosen that optimized the agreement between calculated and experimental data for ground state hematite and maghemite. The XAS calculations reproduce most features in the ground state spectra (**Figs. 3c, 3e & S16**). However, there are evident discrepancies in lineshape broadening and energy position that are greater in magnitude than the transient differences observed in the time-resolved spectra. Consequently, the goal of the simulation study was not to reproduce precisely the ΔXA data but to test whether small-polaron formation is a plausible interpretation of the observed lineshapes.

We calculated theoretical ΔXA spectra for reduced Fe sites in hematite and maghemite with or without the structural distortion predicted by simulation (**Figs 3d & 3f**). For both phases, the calculations predicted that small polaron formation significantly enhanced the intensity of the key feature of the transient spectra. We sought to understand the structural origin of this feature (**Fig. S16**), finding it to be highly sensitive to the Fe-O bond length (**Fig. 3c, inset**). As illustrated in **Figure 1**, bond length expansion is the major predicted feature of small-polaron formation, with a ~4% increase in hematite.

The maghemite phase contains iron in both octahedral and tetrahedral coordination with oxygen. The *ab initio* simulations predict a small (~10 meV) energetic stabilization energy for Fe_{oct}^{2+} *vs.* Fe_{tet}^{3+} sites, suggesting that electrons in the maghemite lattice will access both sites at room temperature. Accordingly, we investigated the contribution from tetrahedral sites to the transient spectra. As shown in **Fig. S18**, the contribution from tetrahedral iron sites is essential to reproduce optimally the lineshape of both ground state and transient spectra. Best agreement was obtained for approximately 30% Fe_{tet}^{2+}, in close quantitative agreement with the DFT results. Thus, the site specificity of transient ΔXA spectra demonstrates that electron conductivity in maghemite occurs via both octahedral and tetrahedral sites. In summary, the experimental ΔXA data indicate that structural relaxation must accompany iron reduction, and the simulation studies show that the bond-length expansion predicted for small-polaron formation leads to the enhancement of the dominant feature observed in the experimental transient X-ray spectra. For two phases, therefore, inclusion of bond-length expansion improves the agreement between theoretical and experimental transient X-ray spectra.

We used the intensity of the transient ΔXA signal at 7.125 keV to measure changes in the amount of ferrous iron in the samples on the nanosecond and microsecond timescales (**Fig. 4)** The ferrous iron concentration exhibits a biphasic decay, initially dropping to ~30% of the initial value within ~2 ns (ferrihydrite and maghemite (**Fig S11b**)) or ~10 ns (hematite). We fitted the nanosecond timescale kinetics data with a three-site model for the location of an electron transferred to a surface iron site following dye excitation, and determined two intrinsic ET rates from fits to the nanosecond kinetics for all phases: k_c, the rate at which electrons at a surface site hop away from the ET site; and k_r, the recombination rate (*c.f.* **Fig. 1a**). For hematite, $k_c = 0.19 \pm 0.04$ ns^{-1}, a value within the range predicted by *ab initio* simulations of small-polaron-mediated electron conduction in bulk hematite[30]. For both ferrihydrite and maghemite $k_c = 0.34 \pm 0.09$ ns^{-1}.

We did not observe detectable differences in any ET properties of maghemite, a well-characterized crystal phase, *vs.* ferrihydrite, a disordered nanomaterial for which the structure is presently a matter of debate[4,31,32]. Ferrihydrite is a nanocrystalline ferric iron oxyhydroxide (*i.e.*, containing iron-ligand polyhedra connected by a mixture of oxo- and hydroxo bridges) lacking long-range order. We have concluded from our own investigations (**Supplementary Information**) that ferrihydrite is composed of the same iron-oxygen polyhedra found in maghemite, predominantly connected by the topology described by the newest model[4], but with extensive stacking and occupational disorder. Our present results show that the electron-hopping rate is determined more by local iron-oxygen topology than long-range order, and that the short-range structure of ferrihydrite and maghemite are very similar. Further insight into the intrinsic electronic properties of these phases is provided by the observation that k_r, the recombination rate, is identical for ferrihydrite and maghemite. Since k_r is related to the energetics for interfacial ET, the most likely interpretation is that interfacial ET from the nanoparticle to surface-bound oxidized dye molecules has a negligible energy barrier and that the free energy change is approximately the same for both phases[33]. As the electron acceptor is the same for both phases, this strongly implies that the elementary redox couple $\mathrm{Fe}^{2+}(s)/\mathrm{Fe}^{3+}(s)$, never previously determined by any experimental approach, is identical for maghemite and ferrihydrite.

While performing nanosecond time-resolved XAS we additionally acquired transient XAS data at timepoints from 1.8 μs to nearly 1 ms following each laser excitation. Low intensity transient ΔXA spectra were discernable up to ~5 μs following photoexcitation (**Fig. S11**) and we used a peak-fitting approach to reveal the microsecond timescale rates of ferrous iron loss from ferrihydrite and maghemite (**Fig 4b**). The spectroscopic data indicate that most electrons were eventually lost from the nanoparticles through recombination rather than dissolution. We used a colorimetric assay to measure the net yield of $\mathrm{Fe}^{2+}(aq)$ after continuous 8-hour pump–probe studies (**Fig. S9B**), finding a small proportion (e.g., ~6% in ferrihydrite) of the total iron to have been permanently reduced and dissolved. Assuming a quantum yield of unity for light-initiated ET, we estimate ~1/300 ferrous iron sites generated in ferrihydrite were released into solution (**Supplementary Information**).

Charge separation over microsecond and longer timescales has been observed in dye-sensitized TiO_2 nanoparticles and the slow recombination kinetics were attributed to electron trapping at surface or interior defect states[34]. We implemented a lattice Monte Carlo (MC) simulation to investigate whether the biphasic electron retention in ferric iron oxides could be accounted for by the intrinsic mobility of small polarons, or implied trapping by defect states, or some combination. We simulated electron self-diffusion within and loss from a spherical 3.4-nm iron oxide nanoparticle represented by a *cubic* lattice of iron sites (**Fig. 5**). Electron self-diffusion was treated as a thermally activated, electron exchange reaction from occupied to neighboring unoccupied iron sites. A Metropolis acceptance rule determined the probability of exchange between sites for which the electron affinity was calculated using one of three spherically-uniform models for the interior electrostatic potential[35], $\psi(r)$, averaging the results of 100 simulations[36]. Loss of electrons occurred with a fixed probability at randomly distributed surface sites: these fixed-location "exit channels" were closed following electron loss, representing recombination with a surface-bound dye. Fe^{2+} loss through dissolution was neglected.

We investigated how physical aspects of the simulation affected the predicted electron dynamics, finding two crucial aspects for reproducing the experimentally observed biphasic kinetics (**Fig. 5d**). First, simulations indicated that photoinjected electrons are introduced to surface or near-surface sites; they therefore likely do not travel far into the particle during injection and thermalization. Second, the inclusion of an electropositive $\psi(r)$ and on-the-fly recalculation based on the instantaneous electron distribution significantly improved the agreement with observations. This confirms that the self-diffusion trajectories of electrons transferred to iron (oxyhydr)oxides will be considerably biased by the presence of positively charged species (protons or oxidized dye molecules) at the surface[37], significantly slowing the recombination rate without invoking the presence of structural defect sites.

In conclusion, this work illustrates the observation of transient reduced metal states in solid oxide phases by time-resolved X-ray spectroscopy, confirms their description as small polarons, and quantifies and explains their transport properties at multiple timescales. Furthermore, our approach is invaluable for obtaining the kinetics and mechanisms of redox and catalytic processes in which transient solid-phase metal species are important reaction intermediates.

Methods Summary

Sample synthesis and characterization. Maghemite nanoparticles (~3.4-nm diameter; 300 m^2/g surface area) were formed via the oxidation of magnetite nanoparticles synthesized by an aqueous precipitation method[38]. A modification of this method was used to synthesize ferrihydrite nanoparticles ((*SI*); 330 m^2/g). Hematite nanoparticles (7-nm) were synthesized by a sol-gel method[39]. Nanoparticle size and phase characterization was performed by X-ray powder diffraction, pair distribution function analysis, and transmission electron microscopy (**Figs. S1-2**). Nanoparticle suspensions (2.4 mM Fe) were sensitized by adding 2’7’-dichlorofluorescein (0.5 mM) at pH 4 (**Figs. S3-4**).

Optical transient absorption spectroscopy. We performed transient optical absorption spectroscopy at the Argonne Center for Nanoscale Materials (CNM) using a femtosecond Ti:sapphire oscillator with 520-nm pump wavelength and a 1.7 kHz repetition rate. A small amount of the output is used to generate the white light continuum probe. The remaining 95% pumps an optical parametric amplifier (OPA) to produce the excitation pulses. The OPA produces a tunable femtosecond output from the UV through to the infrared. The two outputs then enter a transient absorption spectrometer (Helios, Ultrafast Systems), where the probe is variably delayed relative to the pump on a mechanical delay line. A spectrograph is used to collect the spectral content of the probe from 440 to 760 nm as a function of delay. The data are chirp-corrected to within 100 fs over this spectral range.

Time-resolved X-ray spectroscopy. Optical-pump–X-ray-probe spectroscopy was performed at beamline 11-ID-D of the Advanced Photon Source. The laser pump pulse was the second harmonic output of a Nd:YLF regenerative amplifier laser (527 nm, FWHM of ~3 ps, repetition rate of 1 kHz, and power at the sample of ~0.6 W). The X-ray probe pulse was the singlet electron bunch (16 mA, FWHM of 160 ps) extracted from the storage ring at 271.6 kHz operated under hybrid timing mode. The pump-probe delay was adjusted with an analog delay generator with a resolution of 0.5 ps (PDL-100A-20NS, Colby Instruments). 500 mL of suspension was circulated through a 550-μm liquid jet and sample fluorescence captured on avalanche photodiode detectors using Soller slit and Mn filters to suppress background. The Fe K-edge X-ray absorption spectra for X-ray pulses before and after the laser pulse were discriminated using a real-time digital averaging card (Agilent). The concentration of dissolved ferrous iron was determined via a ferrozine colorimetric assay on centrifuged suspensions.

Ab initio structure optimization for small-polaron sites. We used the *ab initio* program CRYSTAL09 (ref. 40) to perform energy minimizations of a ferrous site in a hematite lattice with three-dimensional periodic boundary conditions. CRYSTAL builds crystalline orbitals from a linear combination of space-symmetry adapted Bloch functions that are defined in terms of local Gaussian functions carefully chosen to avoid overly diffuse functions. We used all-electron split-valence double-zeta basis sets pre-optimized for use in CRYSTAL. One basis set was used for iron in either the ferrous or ferric states so as not to pre-determine the location of an extra electron in the lattice. The iron basis set was first pre-optimized for hematite, then diffuse exponents and expansion coefficients were optimized for the mixed-valent iron in the octahedral sublattice of the (room temperature) experimental magnetite structure. The oxygen basis was optimized for hematite. All atomic coordinates and lattice parameters of a 2×2×1 hematite supercell were energy minimized using the hybrid functional B3LYP[41]. A subsequent calculation with identical methods making use of these optimized lattice parameters was performed to energy minimize all atomic coordinates with an extra electron localized on one Fe atom; the supercell was charge neutralized using the uniform background charge method.

Calculation of X-ray absorption spectra. Fe K-edge X-ray absorption spectra were calculated using version 8.2 of FEFF, a real-space full multiple scattering (FMS) code. The muffin tin scattering potentials were calculated self-consistently within a 4.9 Å cluster radius. Convergence of the FMS was tested for cluster radii up to 12Å (~600 atoms), finding convergence within a radius of 9Å (~300 atoms). The final states of the X-ray absorption calculations were fully relaxed in the presence of a core hole. For both phases, we found the excited-state binding energies to be overestimated by the default (Hedin-Lundqvist) exchange-correlation potential. Better agreement for the XAS energy scale was obtained using the Dirac-Hara model.

Solid-phase electron-transfer rate model. We fitted ET rate constants to the nanosecond data using a three-site model for the location of an electron transferred to a surface iron site following dye excitation. The fraction of reduced surface sites decays through two processes with different first-order rate constants: (1) recombination with oxidized dye (rate constant k_r) leads to loss of ferrous iron; (2) electron transfer to sites in the nanoparticle interior (rate constant k_c) leads to long-time-scale retention.

$$\mathrm{Fe}^{2+}_{surface} + dye^{+} \xrightarrow{k_r} \mathrm{Fe}^{3+}_{surface} + dye \tag{1}$$

$$\mathrm{Fe}^{2+}_{surface} + \mathrm{Fe}^{3+}_{interior} \xrightarrow{k_c} \mathrm{Fe}^{3+}_{surface} + \mathrm{Fe}^{2+}_{interior} \tag{2}$$

Because electron transfer into the nanoparticle interior leads to microsecond timescale retention, the rates of *interior-to-surface* electron transfer, and of further recombination, cannot be determined from the experimental nanosecond data and are neglected in this simple model. The rate equations for surface and interior iron can then be written analytically:

$$[\mathrm{Fe}^{2+}_{surface}] = [\mathrm{Fe}^{2+}_{surface}]_{t=0} \exp\left[-t\left(k_c + k_r\right)\right] \tag{3}$$

$$[\mathrm{Fe}^{2+}_{interior}] = [\mathrm{Fe}^{2+}_{surface}] \frac{k_c}{k_c + k_r} \exp\left[-t\left(k_c + k_r\right)\right] \tag{4}$$

We fitted the rate equations to the nanosecond data to determine k_c and k_r. We neglect the finite temporal resolution imposed by the 160-ps width of the X-ray pulse. Examples of the fits are given in **Fig. 4a**, and the results are summarized in **Table S1**.

Acknowledgments: Time-resolved X-ray transient spectroscopy was performed at beamline 11-ID-D at the Advanced Photon Source (APS). Laser facilities were provided by the Solar Energy Conversion group of Chemical Sciences and Engineering Division of Argonne National Laboratory, which is funded through New Facility and Mid-scale Instrumentation grants to Lin X. Chen et al. We thank Dr. L. X. Chen, Dr. Guy Jennings and Chuck Kurtz. PDF analysis was performed at beamline 11-ID-B at the APS. Transient absorption spectroscopy was performed at the Argonne Center for Nanoscale Materials (CNM) and we thank Drs. Gary Wiederrecht and David Gosztola. We thank two anonymous reviewers for their comments on this manuscript. This work was supported by the Chemical Imaging program of the U. S. Department of Energy, Office of Science, and Office of Basic Energy Sciences (DOE-BES), under Contract No. DE-AC02-05CH11231. K.M.R. and P.Z. gratefully acknowledge support from DOE-BES Geosciences program to PNNL. C.F. acknowledges support from the Danish Council for Independent Research. Use of the APS and the CNM is supported by DOE-BES under Contract No. DE-AC02-06CH11357.

Correspondence and request for material should be addressed to: bgilbert@lbl.gov

References:

[1] Hansel, C.M., Benner, S.G., & Fendorf, S., Competing Fe(II)-induced mineralization pathways of ferrihydrite. *Environmental Science & Technology* 39 (18), 7147-7153 (2005).

[2] Yanina, S.V. & Rosso, K.M., Linked reactivity at mineral-water interfaces through bulk crystal conduction. *Science* 320 (5873), 218-222 (2008).

[3] Katz, J.E. *et al.*, Observation of transient iron(II) formation in dye-sensitized iron oxide nanoparticles by time-resolved X-ray spectroscopy. *Journal of Physical Chemistry Letters* 1 (9), 1372-1376 (2010).

[4] Michel, F.M. *et al.*, The structure of ferrihydrite, a nanocrystalline material. *Science* 316 (5832), 1726-1729 (2007).

[5] Pedersen, H.D., Postma, D., & Jakobsen, R., Release of arsenic associated with the reduction and transformation of iron oxides. *Geochimica Et Cosmochimica Acta* 70 (16), 4116-4129 (2006).

[6] Buxton, G.V., Rhodes, T., & Sellers, R.M., Radiation-induced dissolution of colloidal haematite. *Nature* 295, 583-585 (1982).

[7] Kay, A., Cesar, I., & Grätzel, M., New benchmark for water photooxidation by nanostructured α-Fe2O3 films. *Journal of the American Chemical Society* 128 (49), 15714-15721 (2006).

[8] Cowley, J.M., Janney, D.E., Gerkin, R.C., & Buseck, P.R., The structure of ferritin cores determined by electron nanodiffraction. . *Journal of Structural Biology* 131, 210-216 (2000).

[9] Cox, P.A., *Transition metal oxides: An introduction to their electronic structure and properties.* . (Oxford University Press, Inc., New York, 2010).

[10] Holstein, T., Studies of polaron motion. 2. The small polaron. *Annals of Physics* 8 (3), 343-389 (1959).

[11] Rosso, K.M. & Dupuis, M., Reorganization energy associated with small polaron mobility in iron oxide. *Journal of Chemical Physics* 120 (15), 7050-7054 (2004).

[12] Alexandrov, A.S. & Mott, N.F., *Polarons and Bipolarons*. (World Scientific, Singapore, 1996).

[13] Djerdj, I. *et al.*, Oxygen self-doping in hollandite-type vanadium oxyhydroxide nanorods. *Journal of the American Chemical Society* 130 (34), 11364-11375 (2008).

[14] Cherepy, N.J., Liston, D.B., Lovejoy, J.A., Deng, H., & Zhang, J.Z., Studies of Photoexcited Electron Dynamics in γ- and α-Fe2O3 Semiconductor Nanoparticles. *Journal of Physical Chemistry B* 102, 770-776 (1998).

[15] Gratzel, M., Photoelectrochemical cells. *Nature* 414 (6861), 338-344 (2001).

[16] Bressler, C. *et al.*, Femtosecond XANES Study of the Light-Induced Spin Crossover Dynamics in an Iron(II) Complex. *Science* 323 (5913), 489-492 (2009).

[17] Chen, L.X., Probing transient molecular structures in photochemical processes using laser-initiated time-resolved X-ray absorption spectroscopy. *Annual Review of Physical Chemistry* 56, 221-254 (2005).

[18] Cannizzo, A. *et al.*, Light-induced spin crossover in Fe(II)-based complexes: The full photocycle unraveled by ultrafast optical and X-ray spectroscopies. *Coordination Chemistry Reviews* 254, 2677-2686 (2010).

[19] Chen, J. *et al.*, Transient structures and kinetics of the ferrioxalate redox reaction studies by time-resolved EXAFS, optical spectroscopy and DFT. *Journal of Physical Chemistry A* 111, 9326-9335 (2007).

[20] Hilgendorff, M. & Sundström, V., Ultrafast electron injection and recombination dynamics of dye sensitized TiO2 particles. *Chemical Physics Letters* 287, 709-713 (1998).

[21] Waychunas, G.A., Apted, M.J., & Brown, G.E., X-ray K-edge absorption-spectra of Fe minerals and model compounds - near edge structure. *Physics and Chemistry of Minerals* 10 (1), 1-9 (1983).

[22] Chen, L.X., Lee, P.L., Gosztola, D., Svec, W.A., & Wasielewski, M.R., Time-resolved energy-dispersive XAS studies of photoinduced electron transfer intermediates in electron donor-acceptor complexes. *Journal of Synchrotron Radiation* 6, 403-405 (1999).

[23] Wilke, M., Farges, F., Petit, P.-E., Brown, G.E., Jr., & Martin, F., Oxidation state and coordination of Fe in minerals: An Fe K-XANES spectroscopic study. *American Mineralogist* 86 (714-730) (2001).

[24] Colombo, U., Gazzarrini, F., & Lanzavecchia, G., Mechanisms of iron oxides reduction at temperatures below 400 degrees C. *Materials Science Engineering* 2 (3) (1967).

[25] Tronc, E., Belleville, P., Jolivet, J.P., & Livage, J., Transformation of ferric hydroxide into spinel by iron(II) adsorption. *Langmuir* 8, 313-319 (1992).

[26] Tang, J., Myers, M., Bosnik, K.A., & Brus, L.E., Magnetite Fe3O4 nanocrystals: Spectroscopic observation of aqueous oxidation kinetics. *Journal of Physical Chemistry B* 107, 7501-7506 (2003).

[27] Ankudinov, A.L., Ravel, B., Rehr, J.J., & Conradson, S.D., Real Space Multiple Scattering Calculation of XANES. *Physical Review B* 58, 7565 (1998).

[28] Gilbert, B. *et al.*, Multiple scattering calculations of bonding and X-ray absorption spectroscopy of manganese oxides. *J Phys Chem A* 107 (16), 2839-2847 (2003).

[29] Della-Longa, S. *et al.*, Direct Deconvolution of Two-State Pump-Probe X-ray Absorption Spectra and the Structural Changes in a 100 ps Transient of Ni(II)-tetramesitylporphyrin. *Inorganic Chemistry* 48 (9), 3934-3942 (2009).

[30] Iordanova, N., Dupuis, M., and Rosso, K. M. , Charge transport in metal oxides: A theoretical study of hematite α-Fe2O3. *Journal of Chemical Physics* 122 (2005).

[31] Rancourt, D.G. & Meunier, J.F., Constraints on structural models of ferrihydrite as a nanocrystalline material. *American Mineralogist* 93 (8-9), 1412-1417 (2008).

[32] Manceau, A., Evaluation of the structural model for ferrihydrite derived from real-space modelling of high-energy X-ray diffraction data. *Clay Minerals* 44 (1), 19-34 (2009).

[33] Gaal, D.A. & Hupp, J.T., Thermally activated, inverted interfacial electron transfer kinetics: High driving force reactions between tin oxide nanoparticles and electrostatically-bound molecular reactants. *Journal of the American Chemical Society* 122, 10956-10963 (2000).

[34] Nelson, J., Haque, S.A., Klug, D.R., & Durrant, J.R., Trap-limited recombination in dye-sensitized nanocrystalline metal oxide electrodes. *Physical Review B* 63 (2001).

[35] Zarzycki, P., Charmas, R., & Szabelski, P., Study of proton adsorption at heterogeneous oxide/electrolyte interface. Prediction of the surface potential using Monte Carlo simulations and 1-pK approach. *J. Comput. Chem.* 25 (5), 704-711 (2004).

[36] Zarzycki, P. & Rosso, K.M., Origin of Two Time-Scale Regimes in Potentiometric Titration of Metal Oxides. A Replica Kinetic Monte Carlo Study. *Langmuir* 25 (12), 6841-6848 (2009).

[37] Mulvaney, P., Swayambunathan, V., Greiser, F., & Meisel, D., Dynamics of interfacial charge transfer in iron(III) oxide colloids. *Journal of Physical Chemistry* 92, 6732-6740 (1988).

[38] Vayssieres, L., Chaneac, C., Tronc, E., & Jolivet, J.P., Size tailoring of magnetite particles formed by aqueous precipitation: An example of thermodynamic stability of nanometric oxide particles. *Journal of Colloid and Interface Science* 205 (2), 205-212 (1998).

[39] Sugimoto, T., Wang, Y., Itoh, H., & Muramatsu, A., Systematic control of size, shape and internal structure of monodisperse a-Fe2O3 particles. *Colloids and Surfaces A* 134, 265-279 (1998).

[40] Dovesi, R. *et al.*, CRYSTAL09 User's Manual (University of Torino, Torino, 2010).

[41] Becke, A.D., Density-functional thermochemistry. III. The role of exact exchange. *Journal of Chemical Physics* 98 (1993).

FIGURES

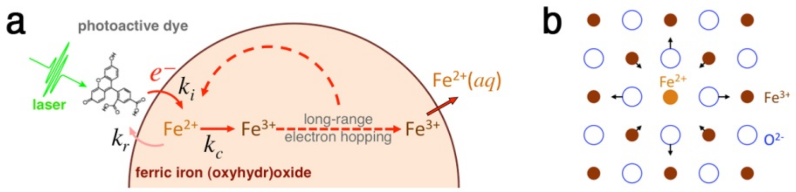

Figure 1. **a**, Scheme of the electron-transfer (ET) pathways following light-initiated interfacial electron transfer from a surface-bound dye molecule to a ferric iron oxide or oxyhydroxide nanoparticle in aqueous suspension. The electron-transfer rate constants, k_i, k_r, k_c, are, the electron-transfer rate constants for interfacial ET, recombination, and internal conduction by hopping to an adjacent iron neighbor respectively. **b**, Illustration of the local structural distortion created by the reduction of a ferric iron site.

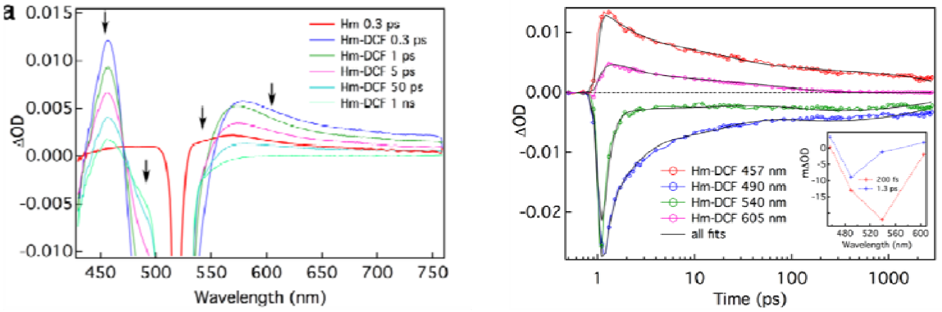

Figure 2. **a** Optical transient absorption (TA) spectrum of uncoated hematite (Hm) at 0.3 ps delay after photoexcitation at 520 nm compared with TA spectra of 2',7'-dichlorofluorescein-coated hematite nanoparticles (Hm-DCF) at the indicated delays. Arrows indicate the wavelengths at which kinetics curves in (b) were extracted. **b**. Transient kinetics observed for uncoated and 27DCF-coated hematite nanoparticles at 457 nm (attributed to absorption of oxidized 27DCF), 490 nm (ground state bleach of 27DCF), 540 nm (stimulated emission of photoexcited 27DCF and ground state bleach); and 605 nm (excited state transitions of trapped photoelectrons generated by band-gap absorption in the nanoparticles, independent of the dye). Also plotted are best-fit transients obtained by global analysis of the Hm-DCF curves with 3 time constants and one offset. The time axis was shifted 1 ps for plotting on a logarithmic scale. **Inset** Wavelength-dependent amplitudes of the two fastest decay time constants: The transient spectrum that decays in the first 200 fs is consistent with stimulated emission from the photoexcitated state of the dye, and indicates that interfacial electron transfer occurs on this time scale. The 1.3-ps spectrum is associated with ground state bleach of the dye and thus represents early interfacial recombination on this time scale. Ground state absorption and emission spectra are given in **Fig. S3.**

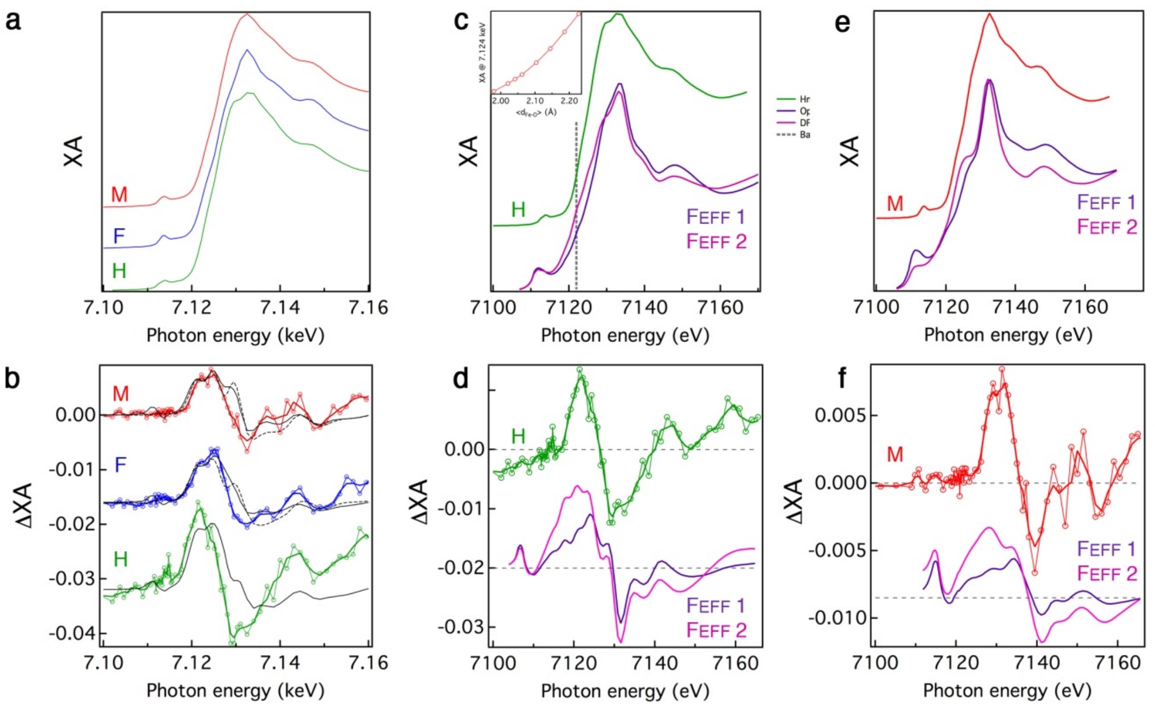

Figure 3. Iron K-edge X-ray absorption (XA) spectroscopy observation of reduced iron sites in three phases of iron (oxyhydr)oxide nanoparticles: maghemite (M), ferrihydrite (F) and hematite (H). **a**, ground state XA spectra of 2',7'-dichlorofluorescein (27DCF) sensitized nanoparticles in suspension. **b**, difference (ΔXA) spectra acquired at 150 ps following light-initiated electron transfer (ET). The raw (markers) and 3-point smoothed (thick lines) data are compared with model spectra obtained by combining the ground-state reference with either a magnetite reference (dashed black lines) or a copy of the ground state spectrum shifted -1.4 eV to simulate valence change without structural relaxation (solid black lines). **c**, Comparison of the experimental Fe K-edge XA spectra for hematite with calculated spectra for a normal ferric iron site hematite (FEFF 1) and for a locally distorted small polaron site in hematite (FEFF 2) obtained from *ab initio* structure

prediction. **Inset**, The calculated on-threshold intensity exhibits high sensitivity to first-shell Fe-O bond length. **d**, Comparison of the transient hematite ΔXA spectrum with calculated spectra for reduced sites without structural relaxation (FEFF 1) and for reduced and structurally distorted sites (FEFF 2). **e, f** compare equivalent experimental and simulated spectra for the maghemite phase.

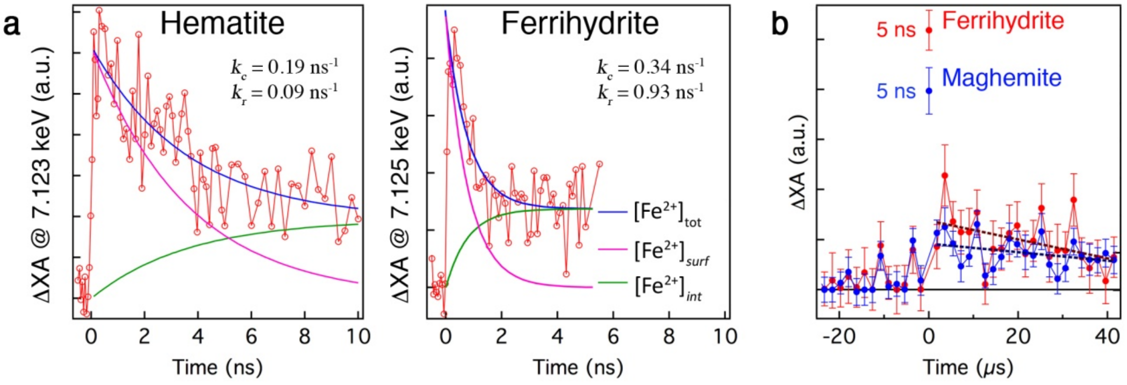

Figure 4. Time-dependence of the lifetime ferrous iron in iron (oxyhydr)oxide nanoparticles at the nanosecond and microsecond timescales. **a**, Experimental kinetics curves showing the creation and loss of ferrous iron in hematite and ferrihydrite nanoparticles. Maghemite nanosecond kinetics data are given in **Fig. S10b**. Fits to a three-site, two-exponential model are used to obtain k_c and k_r. Errors in the fitted constants are 0.05 ns^{-1} or less. **b**, Experimental kinetic curves showing the presence and continued loss of ferrous iron at the microsecond timescale, compared to the ferrous iron signals at 5 ns.

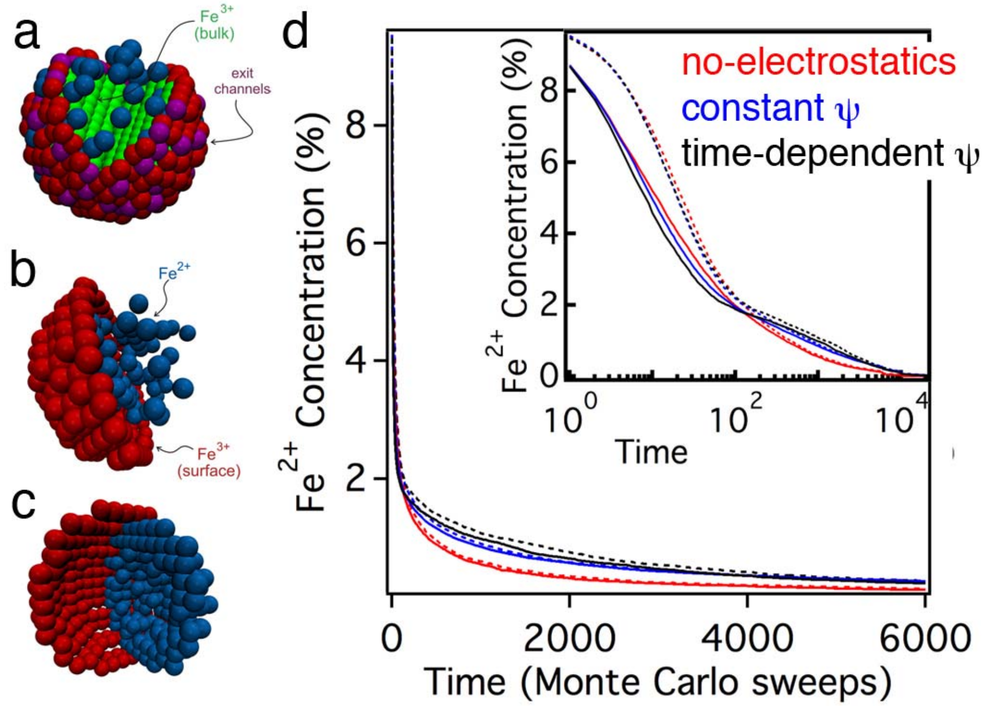

Figure 5. Summary of lattice Monte Carlo (MC) simulations of the concentration and spatial distribution of ferrous iron sites introduced in a model maghemite nanoparticle. The Fe^{2+} sites were initially distributed randomly among either (i) all lattice sites (dashed lines in **d**) or (ii) only subsurface sites (solid lines). Three models for the internal electrostatic potential, $\psi(r)$, derived from surface protonation at pH 4 were compared to evaluate this influence on Fe^{2+} mobility: (i) no surface potential (red lines in **d**), (ii) a constant surface potential (blue lines), or (iii) a time-dependent potential (black lines) obtained by solving the Poisson equation on-the-fly, including the instantaneous distribution of interior electrons. **a**, Depiction of the model nanoparticle, sectioned to reveal interior iron sites. Color key: surface Fe^{3+} (red), interior Fe^{3+} (green), Fe^{2+} (blue), surface Fe^{3+} bound to photooxidized dye molecules ("exit channels"; purple). **b**, Example distribution of initially

internal Fe^{2+} sites. **c**, Example distribution of initially near-surface Fe^{2+} sites. **d**, MC results showing the time-dependence of the interior Fe^{2+} concentration for the six MC configurations, displayed on linear and logarithmic MC time axes. In all cases, the Fe^{2+} decay shows two distinct kinetic regimes, but biphasic decay is more evident for the near-surface initial distribution of Fe^{2+}. Moreover, Fe^{2+} sites exhibit longer transient lifetimes when the electrostatic calculations of site electron affinities use the most accurate time-dependent model.